

# Building a Risk Prediction Model for Postoperative Pulmonary Vein Obstruction via Quantitative Analysis of CTA Images

Yuchen Pei <sup>1</sup>, Guocheng Shi, Wenjin Xia, Chen Wen <sup>1</sup>, Dazhen Sun, Fang Zhu <sup>1</sup>, Jiang Li, Zhongqun Zhu, Xiaoqing Liu, Meiping Huang, Yu-Ping Wang <sup>2</sup>, *Senior Member, IEEE*, Huiwen Chen, and Lisheng Wang <sup>1</sup>

**Abstract**—Total anomalous pulmonary venous connection (TAPVC) is a rare but mortal congenital heart disease in children and can be repaired by surgical operations. However, some patients may suffer from pulmonary venous obstruction (PVO) after surgery with insufficient blood supply, necessitating special follow-up strategy and treatment. Therefore, it is a clinically important yet challenging problem to predict such patients before surgery. In this paper, we address this issue and propose a computational framework to determine the risk factors for postoperative PVO (PPVO) from computed tomography angiography (CTA) images and build the PPVO risk prediction model. From clinical experiences, such risk factors are likely from the left atrium (LA) and pulmonary vein (PV) of the patient. Thus, 3D models of LA and PV are first reconstructed from low-dose CTA images. Then, a feature pool is built by computing different morphological features from 3D models of

LA and PV, and the coupling spatial features of LA and PV. Finally, four risk factors are identified from the feature pool using the machine learning techniques, followed by a risk prediction model. As a result, not only PPVO patients can be effectively predicted but also qualitative risk factors reported in the literature can now be quantified. Finally, the risk prediction model is evaluated on two independent clinical datasets from two hospitals. The model can achieve the AUC values of 0.88 and 0.87 respectively, demonstrating its effectiveness in risk prediction.

**Index Terms**—Congenital heart disease, risk factors, risk assessment model, quantitative computing, computed tomography angiography (CTA).

## I. INTRODUCTION

TOTAL anomalous pulmonary venous connection (TAPVC) is a rare and heterogenous anomaly, accounting for  $\approx 1\%$  to  $3\%$  cases of congenital heart diseases [1]. It is characterized by a failure of the pulmonary venous confluence to be absorbed into the dorsal portion of the left atrium (LA), as illustrated in Fig. 1(a). Historically, TAPVC has led to a high mortality rate of  $\approx 80\%$  in the first year of life without intervention [3]. For the past few decades, advances in surgical techniques and improvement in diagnostic accuracy have contributed to a significant decrease in preoperative mortality. The surgical operation for TAPVC is shown in Fig. 1(b), in which the roof of LA and the common PV are exposed and a side-to-side anastomosis is needed to complete. Several risk factors such as neonatal surgical repair, preoperative pulmonary venous obstruction (PVO), mixed anatomic variation, single-ventricle physiology, and heterotaxy remain to be important for poor prognosis of TAPVC repairing [4]–[7]. Particularly, late mortality after the repair of TAPVC is frequently associated with postoperative pulmonary venous obstruction (PPVO). Patients with PPVO will suffer from insufficient blood supply. Thus there is a higher mortality rate in patients who develop PPVO. Their 30-day, 1-year, and 3-year survival rates are 95.8%, 62%, and 58.7%, respectively [11]. While the total rate of PPVO is  $\approx 15\%$  [8], 5%-18% of the need for reoperation after TAPVC repair is due to PPVO [9], [10]. Thus, PPVO after TAPVC repair poses an ongoing challenge and is associated with increased late mortality and morbidity [12], [13].

Manuscript received March 30, 2021; revised September 7, 2021, November 11, 2021, and January 11, 2022; accepted January 18, 2022. Date of publication January 27, 2022; date of current version July 4, 2022. This work was supported in part by the National Natural Science Foundation of China under Grants 12090024, 81970267, and 81801777, in part by the Shanghai Jiao Tong University School of Medicine Funds under Grants DLY 201815 and ZH2018ZDA24, in part by Shanghai Municipal Science and Technology Major Project under Grant 2021SHZDX0102, and in part by Shanghai Jiao Tong University Translational Medicine Cross Research Funds under Grant YG2022QN094. (Corresponding authors: Lisheng Wang; Huiwen Chen.)

Yuchen Pei, Wenjin Xia, Dazhen Sun, Jiang Li, and Lisheng Wang are with the Department of Automation, Shanghai Jiao Tong University, Shanghai 200240, China, and also with the Key Laboratory of System Control and Information Processing, Ministry of Education, Shanghai 200240, China (e-mail: ychenp0024@gmail.com; kevinxwj@live.cn; giveshot@sjtu.edu.cn; bigpyj@sjtu.edu.cn; lswang@sjtu.edu.cn).

Guocheng Shi, Chen Wen, Fang Zhu, Zhongqun Zhu, and Huiwen Chen are with the Department of Cardiothoracic Surgery, Congenital Heart Center, Shanghai Children's Medical Center, Shanghai Jiao Tong University School of Medicine, Shanghai 200127, China (e-mail: shiguocheng@scmc.com.cn; wenchen1993@sjtu.edu.cn; dr.zhufang@gmail.com; zhuzhongqun@scmc.com.cn; chenhuiwen@scmc.com.cn).

Xiaoqing Liu is with the Deepwise AI Lab, Beijing 100080, China (e-mail: xiaoqing.liu@ieee.org).

Meiping Huang is with the Department of Catheterization Lab, Guangdong Cardiovascular Institute, Guangdong Provincial Key Laboratory of South China Structural Heart Disease, Guangdong Provincial People's Hospital, Guangdong Academy of Medical Sciences, Guangzhou 510055, China (e-mail: huangmeiping@126.com).

Yu-Ping Wang is with the Biomedical Engineering Department, Tulane University, New Orleans, LA 70118 USA (e-mail: wyp@tulane.edu).

Digital Object Identifier 10.1109/JBHI.2022.3146590

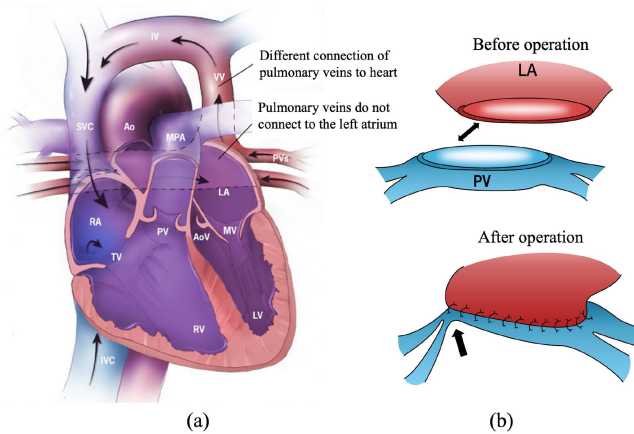


Fig. 1. (a) Anatomy description of total anomalous pulmonary venous connection (TAPVC) [2]. (b) Illustration of operation process: the roof of the left atrium (LA) and the common pulmonary vein (PV) are exposed and a side-to-side anastomosis is completed.

For patients with PPVO, the current standard of care is a follow-up reoperation in time. They should be monitored carefully after TAPVC repair and actively examined on the slightest suspicion of PPVO. During the follow-up process, clinicians can find patients with PPVO symptoms in time and provide effective and necessary treatment, such as the reoperation. Hence, it is significant for clinicians to determine which patients are particularly at the risk of developing PPVO, which is however a complicated task with few studies existed. To this end, in this paper we will address this issue and propose a computational framework to screen the risk factors for PPVO from computed tomography angiography (CTA) images and build the PPVO risk prediction model.

In the past several years, researches have studied risk factors for the survival and outcome of TAPVC surgery. Karamlou *et al.*, [12] reported that patients of younger ages appears to have more emergency operations. Jenkins *et al.*, [14] found that the size of the individual pulmonary vein (PV) is an important predictor of diagnosis and survival for neonates with TAPVC. Bando *et al.*, [6] also found that a small venous confluence and diffuse pulmonary venous narrowing are the risk factors for death. Seale *et al.*, [11] discovered that preoperative clinical factors and cardiac morphologic type are important risk factors for PPVO and survival rate. In the study by Shi *et al.* [8], they used competing-risk analysis to discover that preoperative PVO and infracardiac and mixed anatomic variation are associated with PPVO. However, these studies are generally qualitative, only identifying partial risk factors related to PPVO. As a result, a quantitative and accurate risk predictive model with the determination of risk factors is needed so that clinicians can judge which patient is at risk of PPVO. Recently, deep learning techniques have demonstrated excellent performance in classification and segmentation tasks [15]. [16], [17] proposed to use convolutional neural network to automatically extract image features from CT images and combined them with clinical features in an end-to-end trainable manner to predict PPVO. However, the image features used to predict PPVO are difficult

to understand and cannot provide clinicians with understandable risk factors.

Recently, several risk assessment approaches for adverse cardiac events have been developed. The CARPREG score for women with congenital heart disease, acquired heart disease, and arrhythmia was first introduced [18]. Puchner *et al.*, [19] demonstrated that high-risk coronary plaque features detected from CTA can improve the diagnostic accuracy in identifying patients with acute coronary syndromes and the presence of significant coronary artery disease for patients with acute chest pain. In [20], the investigators studied the quantitative coronary wall volume change to assess the heart transplanted patients based on coronary CTA. In [21], the study sought to outline the natural history of ascending thoracic aortic aneurysm based on ascending aortic length and developed novel predictive tools to aid in risk stratification. Overall, the risk assessment models described above can help clinicians to stratify patients into distinct prognosis groups and predict outcomes. Despite of these efforts, there is still no risk assessment model for PPVO in TAPVC patients.

While radiomics technique is widely applied in various tumor studies [22]–[24], it was until recently that it has been applied to cardiac image analysis [25]–[28]. By the radiomics analysis [29], a feature pool is first constructed from medical images. Then, risk factors are selected from the feature pool, and finally a risk prediction model is built. Cetin *et al.*, [25] demonstrated a new approach to identify cardiovascular diseases from cine-MRI by computing radiomic image features. Oikonomou *et al.*, [28] presented a high-risk radiomic signature of coronary perivascular adipose tissue from the analysis of traditional coronary CTA scans. These results indicate that radiomics features of cardiac images can indeed provide feasible assistance for clinicians. However, similar researches are not seen in PPVO prediction because of the complexity of constructing a suitable feature pool for PPVO analysis.

Based on clinical experiences and reports in [6], [8], [11], [12], [14], infracardiac and mixed anatomic variations are associated with PPVO in patients with TAPVC. In particular, the morphological structures of LA and PV and their spatial relationship are closely related to PPVO. However, these are only qualitative observations from clinic, and how LA and PV influence the PPVO quantitatively is not clear. To solve this problem, we propose a computational framework to screen the risk factors for PPVO from CTA images, with the construction of risk predictive model. First, we segment LA and PV from CTA images and reconstruct their 3D models. Then, a feature pool is constructed, which consists of various morphological features from LA and PV, such as the volume of LA, length of common PV, mean radius of common PV, bifurcation angle of PV branches, spatial distance between PV and LA, and the coupling features of LA and PV. Finally, based on multivariate logistic regression model and machine-learning techniques, four different risk factors for PPVO are determined from the feature pool for the construction of risk prediction model. Compared with [6], [8], [11], [12], [14], quantitative risk factors rather than qualitative observations are provided in this work. In particular, critical risk factors are extracted from CTA images, resulting



Fig. 2. Illustration of our framework for predicting postoperative PVO (PPVO).

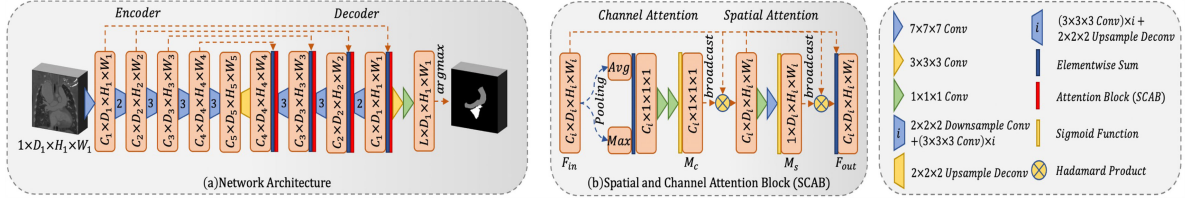


Fig. 3. Illustration of our network architecture for segmenting PV and LA.

in more accurate the risk prediction model. The feature set is constructed by segmenting, modeling and quantitative analysis of LA and PV, which are more suitable for PPVO analysis in comparison with the work in [25], [28]. The risk factors are based on morphological features from LA and PV, promising for better repeatability and interpretability of the prediction model than those in tumor radiomics analysis. Finally, the proposed risk prediction model is evaluated with two independent clinical datasets from two different hospitals, which achieves the area under curve (AUC) values of 88% and 87% respectively, demonstrating its effectiveness.

The contributions of this paper can be summarized as follows:

- An effective risk prediction model is proposed for PPVO in TAPVC patients, and quantitative morphological risk factors are extracted from CTA images.
- A computational framework is proposed to quantify risk features from the CTA images, which are often observed qualitatively and ambiguously in the literature.
- A novel set of quantitative morphological features are defined to describe spatial relationship between LA and PV, which are often overlooked by conventional studies but contribute to important patterns.

The remaining part of this paper is organized as follows. In Section II, the proposed method are described. Results, discussions, and conclusions are presented in Sections III, IV, and V, respectively.

## II. METHOD

In this section, we introduce the proposed framework in detail, whose diagram is shown in Fig. 2. First, we describe the segmentation and 3D modeling of LA and PV. Then we construct a feature pool by computing a series of morphological features from the 3D models of LA and PV. Finally, we determine risk factors from the feature pool and build a risk assessment model for PPVO. This retrospective study was conducted following ethical approval from the Institutional Review Board at the Shanghai Children’s Medical Center and Guangdong’s Provincial People’s hospital.

### A. Segmentation and 3D Modeling of LA and PV

From clinical experiences, the PPVO is closely associated with morphological structures of LA and PV and their spatial relationship. Thus, we will first segment LA and PV from CTA images and construct their 3D models. In clinics, CTA with low radiation dose (Low-Dose) is commonly used for children imaging, which generates CTA images with lower contrast than general CTA images, as illustrated in Fig. 4(a). This makes it a difficult task to segment LA and PV from Low-Dose CTA, especially in children. About 2 hours will be taken for radiologists to delineate PV and LA manually from a 3D CTA image. Hence, we propose a hybrid strategy to segment PV and LA, in which PV and LA are first segmented automatically from CTA images, and then the segmented result is further modified manually by clinicians. This way combines the automatic image processing and the experience of clinicians, making a trade-off between accuracy and time. It only takes about 20 minutes for a clinician to make corrections, which is acceptable.

1) *Automatic Segmentation of LA and PV*: V-Net [30] is a convolutional neural network widely used in 3D medical image segmentation tasks due to its good performance and low computational cost. We have improved the V-Net in [31] to automatically segment PV and LA from 3D Low-Dose CTA images of TAPVC children. In the improved architecture, the V-Net is used as the baseline model, and several useful improvements have been made to it. First, we remove the residual connection in the convolution layer of the encoder to avoid over-fitting. Second, since the batch size in 3D images is small, we replace batch normalization with instance normalization in all convolution layers. Most importantly, we incorporate the attention mechanism [32] into the V-Net by implementing the attention mechanism in spatial and channel attention blocks (SCABs). The SCABs can guide the decoder to focus on the important spatial position and feature channels to extract more useful features to obtain better segmentation performance. The improved V-Net architecture is called SCAB-VNet. The network architecture is shown in Fig. 3.

Firstly, the OTSU threshold method [33] is used to segment the region of the lung from the whole 3D CTA images to save computational time. Then the CTA images are normalized

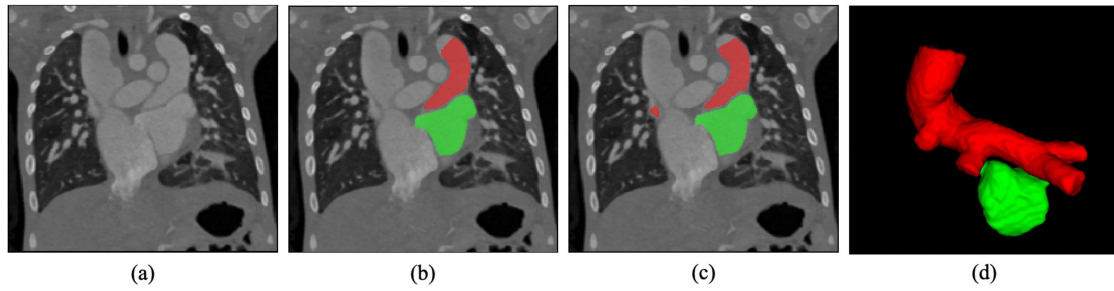


Fig. 4. Illustration of segmentation and 3D modeling of PV and LA from CTA images. (a) Original CTA image. (b) Automatic segmentation of PV and LA, masked by red and green, respectively. (c) PV and LA areas after manual revision of clinicians. (d) 3D modeling of PV and LA.

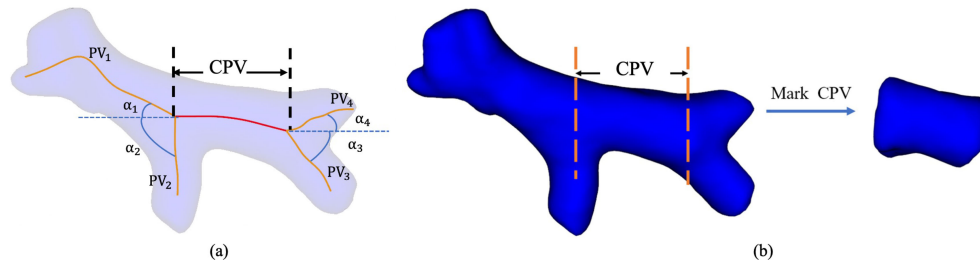


Fig. 5. (a) A PV consists of a common PV (CPV) and four branches:  $PV_i, i = 1, 2, 3, 4$ .  $\alpha_i$  represents the angle between branch of  $PV_i$  and the centerline of the CPV. The red curve represents the centerline of the CPV, the yellow curves represent the centerlines of four branches of PV. (b) The CPV marked from the PV model by clinicians and the separated CPV model.

by the Z-score method. Finally, CTA images are fed into the SCAB-VNet to segment LA and PV. From our experiment, the automatic segmentation can correctly recognize most of the voxels belonging to LA and PV, as illustrated in Fig. 4(b).

2) *Manual Revision*: Due to the complexity of PV and LA in Low-Dose CTA, the segmentation of PV and LA cannot reach 100% accuracy by the network, which usually contains some false positive regions or misses some voxels belonging to LA and PV. In this case, many morphological features cannot be computed correctly. The subsequent manual correction is necessary for computing high-precision morphological features. Usually, such manual editing only takes about 20 minutes or so in a CTA image, a very short time as opposed to manual delineations, which is about two hours or so. Based on this hybrid strategy, both the accuracy and time can be balanced, facilitating clinicians' work in analyzing PV and LA quantitatively.

3) *3D Models of LA and PV*: In order to generate smoothed surface models of PV and LA, the segmentation results of PV and LA will be used as the initialization, and refined by active contour models [34]. Subsequently, the marching cube algorithm [35] is used to reconstruct the surface models of LA and PV from the binary segmentation results as shown in Fig. 4(d).

## B. Computation of Morphological Features From LA and PV

For risk factors of PPVO, clinicians have suggested some qualitative but ambitious measurements from their clinical experiences. In this section, we will show how to quantify them more accurately by morphological features from LA and PV.

The morphological features and their coupling features together to form the feature pool.

1) *Morphological Features From PV and LA*: PV vessel consists of a common PV (CPV) and four branches, as shown in Fig. 5(a). Considering that CPV is a complicated section of PV and varied in different patients, its position is manually marked by experienced clinicians from visualized PV model. As a result, its 3D model is separated from the PV model, as shown in Fig. 5(b). Based on the suggestions of clinicians, the following features of CPV and LA are considered: the volume of LA, length of CPV, mean radius of CPV, tortuosity of CPV, bifurcation angles between CPV and four branches of PV. In order to quantitatively describe these features, the centerline of the PV vessel should be first extracted from the PV model. In this work, the centerline is computed by the method in [36], which has low computational complexity. An example of centerlines extracted from a PV model is illustrated in Fig. 5(a). The length and tortuosity of the centerline of CPV are denoted by  $|CPV|$  and  $Tor(CPV)$ , respectively. CPV has varied radii at different positions along its centerline, and the average radius is denoted by  $R(CPV)$ . Let  $PV_1, PV_2, PV_3, PV_4$  represent the centerlines of the four branches of the PV as shown in Fig. 5(a). The four angles between the four branches of PV and the centerline of the CPV are denoted by  $\alpha_1, \alpha_2, \alpha_3, \alpha_4$ , respectively. Then morphological features from PV and LA can be calculated as follows:

$V_{LA}$ : The volume of LA, estimated by counting voxels in the segmentation area of LA.

$V_{CPV}$ : The volume of CPV, estimated by counting voxels in the segmentation area of CPV, as shown in Fig. 5(b).

$|CPV|$ : The length of the centerline of CPV.

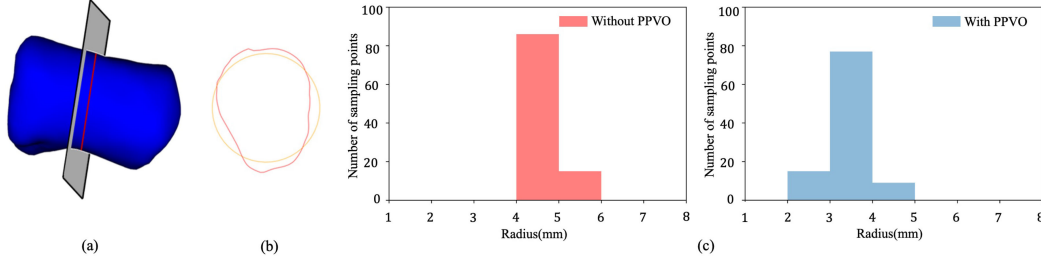


Fig. 6. Illustration of the CPV radius computation. (a): A plane perpendicular to CPV is computed. (b): A circle (yellow) is used to fit the intersecting curve (red) between the CPV model and the plane. (c): Distribution histograms of CPV radii from a patient without PPVO and a patient with PPVO.

$\alpha_i = \Theta(\overrightarrow{PV_i}, \overrightarrow{CPV})$ ,  $i = 1, 2, 3, 4$ , represent the angle between two vectors  $\overrightarrow{PV_i}$  and  $\overrightarrow{CPV}$ .  $\overrightarrow{PV_i}$  and  $\overrightarrow{CPV}$  represent the principal direction of  $PV_i$  and CPV, respectively.

$Tor(CPV)$ : Let  $Dist|CPV|$  denote the distance between two vertices of the CPV centerline. The tortuosity of CPV is approximately computed as follows:

$$Tor(CPV) = \frac{|CPV|}{Dist|CPV|} - 1 \quad (1)$$

The tortuosity defined above is zero when the vessel is straight, and increases when the vessel is more tortuous.

$R(CPV)$  is computed from the CPV model as follows:

Firstly, the centerline of CPV is discretely sampled at 100 points at equal intervals. Secondly, the radius is computed at each sampling point. At each sampling point, a plane perpendicular to CPV is computed and used to calculate an intersecting curve between this plane and the surface model of CPV, as shown in Fig. 6(a). Since the actual PV is not a regular circular tube, the intersection curve is fitted with a circle and the radius of this circle is used at the sampling point, as shown in Fig. 6(b). We utilize the average radius and variance of the CPV radii computed from 100 sampling points to depict CPV thickness as follows:

$$R(CPV) = \frac{\sum_{i=1}^{100} r(P_i)}{100} \quad (2)$$

$$VAR_{R(CPV)} = \frac{\sum_{i=1}^{100} (r(P_i) - R(CPV))^2}{100 - 1} \quad (3)$$

where  $r(P_i)$  represents the radius at the sampling point  $P_i$ . In Fig. 6(c), the distribution of two patient's CPV radii computed at different sampling points are shown, indicating that the thickness of a CPV can be approximately described by its average radius.

**2) Features for Describing Distance Between LA and CPV:** Among the TAPVC operation, CPV and LA will be pulled together along a direction (denoted by  $Dir$ ) and stitched together along an incision of CPV, as shown in Fig. 1(b). Thus, TAPVC operation's result is closely related to the distance between LA and CPV (DBLP). Along the direction  $Dir$ , each point in the centerline of CPV will have the corresponding projection point on LA surface model, and a projection distance can thus be determined. DBLP actually can be regarded as the distribution of all such projection distances from the centerline of CPV to the surface of LA. Since the spatial relationship between LA and CPV is very complicated, DBLP is difficult to describe

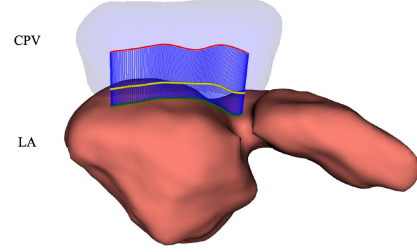


Fig. 7. Illustration of projection distances distribution between LA and CPV (DBLP). The red curve represents the centerline of the CPV from which 100 points are sampled and 100 lines (blue) are projected onto LA surface. 100 intersecting points between the projected lines and CPV surface (or LA surface) are represented in yellow (green).

based only on the minimal or mean distance. In the following, the DBLP will be quantitatively measured by histogram-based features.

We will first estimate the direction  $Dir$  from the surface models of LA and CPV. Similar to Section II-B(1), 100 discrete sampling points of the centerline of CPV can be computed. For each sampling point  $P_i$ ,  $i = 1, 2, \dots, 100$ , we can compute a point  $Q_i$  from the surface model of LA such that the distance between  $P_i$  and  $Q_i$  is the shortest among all possible distances between  $P_i$  and LA. Thus, for each sampling point, we can determine a direction from  $P_i$  to  $Q_i$ , denoted by a vector:  $\overrightarrow{P_i Q_i}$ . The average of such vector directions of all sampling points will approximately represent the direction  $Dir$ :

$$Dir = \frac{\sum_{i=1}^{100} \overrightarrow{P_i Q_i}}{100} \quad (4)$$

For each sampling point, we can compute its projection point over the LA surface model along with the direction  $Dir$ , and the distance between these two points can be obtained. Consequently, a distance distribution histogram is generated based on such projection distances of all sampling points on the centerline of CPV as shown in Fig. 7, where DBLP is intuitively illustrated by all blue lines. The  $d_{ave}$  represents the average distance between the CPV and LA, defined as follows:

$$d_{ave} = \frac{\sum_{i=1}^{100} d_{Dir}(P_i, LA)}{100} \quad (5)$$

$$VAR_{d_{ave}} = \frac{\sum_{i=1}^{100} (d_{Dir}(P_i, LA) - d_{ave})^2}{100 - 1} \quad (6)$$

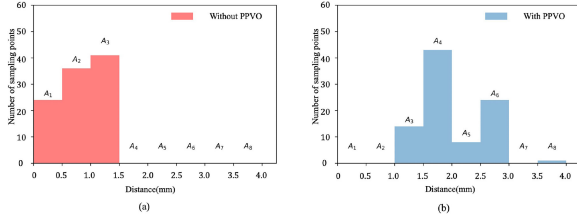


Fig. 8. DBLP Histograms of two patients. (a) Without PPVO, (b) with PPVO.

where  $d_{Dir}(P_i, LA)$  represents the distance from the sampling point  $P_i$  to the LA along the direction  $Dir$ .  $d_{ave}$  and  $VAR_{d_{ave}}$  represent the average value and variance of all projection distances of the DBLP. DBLP histogram, a quantitative description of distance change between LA and CPV, is constructed as follows. The horizontal axis represents the projection distance value with the unit of  $0.5\text{ mm}$  and ranging from  $0\text{ mm}$  to  $4\text{ mm}$  shown in Fig. 8. The vertical axis represents the number of sampling points with the corresponding value of projection distance. Consequently, the DBLP histogram is divided into 8 bins, as shown in Fig. 8. Let  $A_1, A_2, \dots, A_8$  represent sampling points of 8 different bins respectively, and  $D_i = \frac{A_i \times |CPV|}{100}$ ,  $i = 1, 2, \dots, 8$ . The values of  $D_1, \dots, D_8$  represent the lengths of different CPV segments, whose projection distances are in  $0\text{ mm} - 0.5\text{ mm}, \dots, 3.5\text{ mm} - 4\text{ mm}$ , respectively. For instance,  $D_1$  represents the length of CPV segment whose projection distance is within  $0\text{ mm} - 0.5\text{ mm}$ . Fig. 8 presents DBLP histograms of two patients without and with PPVO, showing that the DBLP varies between different patients and cannot be described by  $d_{ave}$ . This is the reason that we use the DBLP histogram to describe the spatial relationship between LA and CPV for each patient.

Clinically, the longer the CPV segment with smaller projection distances, the more conducive to the success of the operation. Thus, we further derive additional quantitative features as follows:

$$\begin{aligned}
 D_9 &= D_8 + D_7 \\
 D_{10} &= D_8 + D_7 + D_6 \\
 D_{11} &= D_8 + D_7 + D_6 + D_5 \\
 D_{12} &= D_1 + D_2 \\
 D_{13} &= D_1 + D_2 + D_3 \\
 D_{14} &= D_1 + D_2 + D_3 + D_4
 \end{aligned} \quad (7)$$

$D_9, D_{10}, D_{11}$  depict the lengths of different CPV segments whose projection distances are in  $3\text{ mm} - 4\text{ mm}$ ,  $2.5\text{ mm} - 4.0\text{ mm}$ ,  $2.0\text{ mm} - 4.0\text{ mm}$ , respectively.  $D_{12}, D_{13}, D_{14}$  depict the lengths of different CPV segments whose projection distances are in  $0.0\text{ mm} - 1.0\text{ mm}$ ,  $0.0\text{ mm} - 1.5\text{ mm}$ ,  $0.0\text{ mm} - 2.0\text{ mm}$ , respectively. Roughly speaking, if  $D_{12}$ , or  $D_{13}$ , or  $D_{14}$  has larger value, DBLP can be regarded to be small.

3) **Coupling Features Between LA and PV:** From clinical experience, TAPVC operation's outcome is greatly affected by coupling features between LA and CPV. For example, when

CPV is thick and long, a patient might have PPVO if the distance between LA and CPV is large. Thus, we will construct some coupling features to quantitatively describe such a coupling relationship between LA and CPV. The coupling features will be formed by three different kinds of features: various DBLP features  $D_j$  ( $j = 1, 2, \dots, 14$ ), the CPV length  $|CPV|$ , and the mean radius of CPV  $R(CPV)$ . We compute the following coupling features:

$$C_1 = |CPV| \times R(CPV) \times d_{ave}$$

$$C_{j+1} = |CPV| \times R(CPV) \times D_j, \quad (j = 1, \dots, 14) \quad (8)$$

where  $C_2, \dots, C_{15}$  describe various coupling among various DBLP features, CPV thickness, and CPV length. Since  $\pi \times |CPV| \times R(CPV)^2$  is an approximation to the volume of CPV, the volume of CPV ( $V_{CPV}$ ) is also incorporated into coupling features. Additional coupling features are constructed based on the volume of CPV as follows:

$$C_{16} = V_{CPV} \times d_{ave}$$

$$C_{j+16} = V_{CPV} \times D_j \quad (j = 1, \dots, 14) \quad (9)$$

where  $C_{17}, \dots, C_{30}$  describe the coupling cases between various DBLP features and the CPV volume.  $C_{13}, C_{14}, C_{15}$  can be used to describe the cases where the CPV length, mean radius of CPV are large but the DBLP is small.  $C_{28}, C_{29}, C_{30}$  describe the cases where CPV volume is large but DBLP is small.

We also compute the tortuosity of the projected CPV over LA surface. The projection direction  $Dir$  is computed in equation (4). Let  $\widehat{CPV}$  represent the projected CPV.

$$Tor_{proj}(CPV) = \frac{|\widehat{CPV}|}{Dist|\widehat{CPV}|} - 1 \quad (10)$$

$Dist|\widehat{CPV}|$  denotes the distance between the two vertices of the projected CPV centerline.

Consequently, 57 features are computed or defined in this paper, as shown in Table I, including  $\alpha_1, \dots, \alpha_4, C_1, \dots, C_{30}, Tor(CPV), Tor_{proj}(CPV), D_1, \dots, D_{14}, |CPV|, V_{LA}, V_{CPV}, d_{ave}, R(CPV), VAR_R(CPV)$  and  $VAR_{d_{ave}}$ . These features constitute a feature pool.

### C. Determination of Risk Factors

Risk factors of PPVO are determined from the feature pool by feature selection using a retrospective dataset of children with TAPVC repairing surgery. In the dataset, CTA image and surgery result (with or without PPVO) of each patient will be detailed in Section III. The importance score of each feature computed by random forest [37] is provided in Table I. The correlations between all features to each other are shown in Fig. 9. Fig. 9 shows that many features in the feature pool are highly correlated, indicating that there is redundancy among these features. Thus, it is necessary to select features from the feature pool.

Firstly, a univariable statistical significance test is performed [38], and features with a  $p$ -value  $< 0.1$  are retained from all 57 features for further selection. The commonly used

TABLE I  
FEATURE POOL CONSTRUCTED IN OUR FRAMEWORK

Name	Purpose	Importance Score	$p$ -Value	Name	Purpose	Importance Score	$p$ -Value
$V_{LA}$	Describe the size of LA	0.0326	<0.1	$C_3$	$ CPV  \times R(CPV) \times D_2$	0.0162	<0.1
$V_{CPV}$	Describe the size of CPV	0.0477	<0.1	$C_4$	$ CPV  \times R(CPV) \times D_3$	0.0198	<0.1
$ CPV $	The length of CPV	0.0203	<0.1	$C_5$	$ CPV  \times R(CPV) \times D_4$	0.0174	<0.1
$\alpha_1$	The orientations between a branch of PV and CPV	0.0269	<0.1	$C_6$	$ CPV  \times R(CPV) \times D_5$	0.0116	0.4512
$\alpha_2$	The orientations between a branch of PV and CPV	0.0247	<0.1	$C_7$	$ CPV  \times R(CPV) \times D_6$	0.0128	0.1707
$\alpha_3$	The orientations between a branch of PV and CPV	0.0237	0.1867	$C_8$	$ CPV  \times R(CPV) \times D_7$	0.0093	0.2892
$\alpha_4$	The orientations between a branch of PV and CPV	0.0179	0.4899	$C_9$	$ CPV  \times R(CPV) \times D_8$	0.0086	0.1835
$R(CPV)$	The average radius or thickness of CPV	0.0504	<0.1	$C_{10}$	$ CPV  \times R(CPV) \times D_9$	0.0085	0.4741
$VAR_{R(CPV)}$	The changes of CPV radii	0.0339	0.2691	$C_{11}$	$ CPV  \times R(CPV) \times D_{10}$	0.0114	0.3186
$d_{ave}$	The mean of all projection distances between CPV and LA	0.0217	<0.1	$C_{12}$	$ CPV  \times R(CPV) \times D_{11}$	0.0137	0.4390
$VAR_{d_{ave}}$	The variance of all projection distance between CPV and LA	0.0191	0.2212	$C_{13}$	$ CPV  \times R(CPV) \times D_{12}$	0.0130	<0.1
$Tor(CPV)$	The tortuosity ratio of the CPV	0.0221	0.4055	$C_{14}$	$ CPV  \times R(CPV) \times D_{13}$	0.0183	<0.1
$Tor_{proj}(CPV)$	The tortuosity ratio of the projected CPV over LA	0.0198	0.3666	$C_{15}$	$ CPV  \times R(CPV) \times D_{14}$	0.0216	<0.1
$D_1$	Lengths of CPV segments have 0 – 0.5mm projection distances to LA	0.0149	<0.1	$C_{16}$	$V_{CPV} \times d_{ave}$	0.0207	<0.1
$D_2$	Lengths of CPV segments have 0.5– 1.0mm projection distances to LA	0.0231	<0.1	$C_{17}$	$V_{CPV} \times D_1$	0.0121	<0.1
$D_3$	Lengths of CPV segments have 1.0– 1.5mm projection distances to LA	0.0198	<0.1	$C_{18}$	$V_{CPV} \times D_2$	0.0149	<0.1
$D_4$	Lengths of CPV segments have 1.5– 2.0mm projection distances to LA	0.0144	0.1964	$C_{19}$	$V_{CPV} \times D_3$	0.0189	<0.1
$D_5$	Lengths of CPV segments have 2.0– 2.5mm projection distances to LA	0.0189	0.2393	$C_{20}$	$V_{CPV} \times D_4$	0.0177	<0.1
$D_6$	Lengths of CPV segments have 2.5– 3.0mm projection distances to LA	0.0161	0.1384	$C_{21}$	$V_{CPV} \times D_5$	0.0128	0.3262
$D_7$	Lengths of CPV segments have 3.0– 3.5mm projection distances to LA	0.0131	0.2974	$C_{22}$	$V_{CPV} \times D_6$	0.0121	0.1675
$D_8$	Lengths of CPV segments have 3.5– 4.0mm projection distances to LA	0.0103	0.1800	$C_{23}$	$V_{CPV} \times D_7$	0.0063	0.2546
$D_9$	$D_7 + D_8$	0.0107	0.4835	$C_{24}$	$V_{CPV} \times D_8$	0.0082	0.1745
$D_{10}$	$D_6 + D_7 + D_8$	0.0137	0.2303	$C_{25}$	$V_{CPV} \times D_9$	0.0094	0.4234
$D_{11}$	$D_5 + D_6 + D_7 + D_8$	0.0182	0.2475	$C_{26}$	$V_{CPV} \times D_{10}$	0.0110	0.2751
$D_{12}$	$D_1 + D_2$	0.0136	<0.1	$C_{27}$	$V_{CPV} \times D_{11}$	0.0146	0.3933
$D_{13}$	$D_1 + D_2 + D_3$	0.0156	<0.1	$C_{28}$	$V_{CPV} \times D_{12}$	0.0107	<0.1
$D_{14}$	$D_1 + D_2 + D_3 + D_4$	0.0216	<0.1	$C_{29}$	$V_{CPV} \times D_{13}$	0.0154	<0.1
$C_1$	$ CPV  \times R(CPV) \times d_{ave}$	0.0190	<0.1	$C_{30}$	$V_{CPV} \times D_{14}$	0.0189	<0.1
$C_2$	$ CPV  \times R(CPV) \times D_1$	0.0097	<0.1				

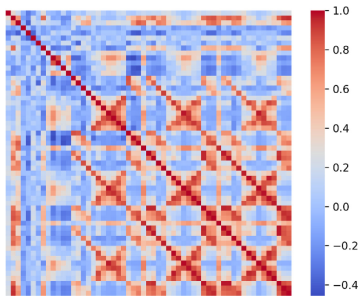


Fig. 9. The correlations between all features in the feature pool. (From left to right:  $V_{LA}$ ,  $V_{CPV}$ , ...,  $C_{30}$ ).

threshold of 0.05 is relaxed to 0.1 to retain a moderate number of features for further investigation. The  $p$ -value of each feature is also shown in Table I. This step retains 29 features.

Secondly, variation inflation factor (VIF) is a statistical measurement used to evaluate the degree of collinearity between features and remove redundant features [39]. The feature with

the highest VIF value is removed, and perform this VIF-filtering procedure recursively until the highest VIF value is below a certain threshold. We have experimented with different thresholds in the set  $\{50, 30, 10, 5\}$  to find a suitable threshold. Under these different thresholds, the number of features filtered by VIF is  $\{18, 15, 12, 10\}$ , respectively. Considering the sample size, we decide 10 as the selected threshold, and therefore 12 features are suitable for further selection.

Finally, the LASSO (least absolute shrinkage and selection operator [40]) regression model is adopted to select important features. The regularization parameter used in the LASSO is searched in a range of  $[10^{-1}, 10^5]$  with a step size of 0.5 in logscale. As shown in Fig. 10, each curve represents the coefficient of the corresponding feature in LASSO model that varies with the regularization parameter. The coefficients of most features are eliminated in  $[10^{-0.5}, 10^{0.5}]$ . So we conduct a further search in this range, using a step size of 0.05 in the logscale. Based on the cross-validation, the performance is the best when the L1-regularization parameter is  $10^{0.3}$ . In this case, only 4 features are left.

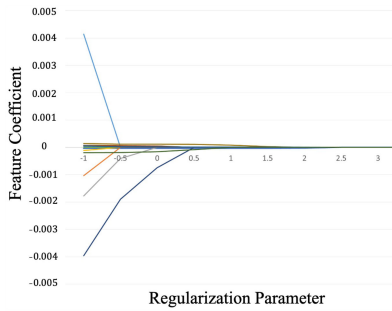


Fig. 10. Coefficient of features in LASSO model under different regularization parameters.

TABLE II  
DATASETS USED IN OUR EXPERIMENT

Source	Dataset	Patient num	With PPVO num
SCMC ( $Data_1$ )	Training	54	14(25.9%)
	Test	14	3(21.4%)
GPPH ( $Data_2$ )	Test	15	6(40%)

(SCMC: Shanghai Children's Medical Center, GPPH: Guangdong's Provincial People's Hospital).

#### D. Risk Prediction Model by Morphological Features of LA and PV

The selected four morphological features are subsequently entered into a multivariable logistic regression model [41] to build a risk prediction model. Considering the small sample size of the dataset, we enforce a mixed L1 and L2 norm based regularization in model fitting. The parameters of the logistic regression model and regularization ratios are decided through 3-fold cross-validation within the training dataset. Consequently, a risk assessment model consisting of four morphological features is generated, which is used for predicting PPVO in TAPVC patients.

### III. RESULTS

In this section, selected risk factors are tested. In addition, the risk prediction model and its performances are evaluated.

#### A. Dataset

Considering potential uncontrollable factors in ages, infants aged 12 months or older were not included in this study. As shown in Table II, 68 patients from Shanghai Children's Medical Center were split into a training and a test dataset. The training dataset includes 54 patients, and 14 of which suffer from PPVO. The test dataset (denoted by  $Data_1$ ) contains 14 patients, and 3 of them suffer from PPVO. In order to verify the generalization of our risk assessment model, the model is additionally evaluated by an independent dataset from Guangdong's Provincial People's hospital (denoted by  $Data_2$ ) with 15 patients including 6 of them have PPVO. In this paper, a patient is diagnosed as having PPVO if postoperative pulmonary venous obstruction (PPVO) occurs within one year after the operation procedure.

#### B. Selected Risk Factors and Risk Prediction Model

Four risk factors are selected for PPVO with the proposed method, including the volume of LA ( $V_{LA}$ ), the volume of CPV ( $V_{CPV}$ ), average radius of CPV ( $R(CPV)$ ) and the coupling feature  $C_{30}$  ( $C_{30} = V_{CPV} \times D_{14}$ , coupled by the volume of the CPV and the length of the CPV segment with small projection distance in  $0mm - 2mm$ ).

Let  $F = [V_{LA}, V_{CPV}, R(CPV), C_{30}]$  represent the vector formed by the values of the four risk factors,  $W = [-0.34324788, -0.09530407, -0.6822308, -0.3734412, ]$  represent the vector formed by the weights of these four risk factors, respectively. The prediction model  $Pre$  for PPVO is then defined as:

$$Pre = \frac{1}{1 + e^{-(-0.34067382 + F^T W)}} \quad (11)$$

By the model, we can estimate the risk probability for each patient based on his/her CTA image, and classify the patient into high-risk or low-risk groups. The prediction model is jointly determined by the weighted sum of the four risk factors.

#### C. Performance of Risk Prediction Model

Let TP, FP, TN, FN represent the true positive, false positive, true negative and false negative, respectively. Then true positive rate (TPR), precision, false negative rate (FNR), recall, accuracy and F1-score are represented as follows:

$$\begin{aligned} TPR = Recall &= \frac{TP}{TP + FN} \\ Precision &= \frac{TP}{TP + FP} \\ FNR &= \frac{FP}{TN + FP} \\ Accuracy &= \frac{TP + TN}{TP + TN + FP + FN} \\ F1 - score &= \frac{2 \times Precision \times Recall}{Precision + Recall} \end{aligned} \quad (12)$$

The ROC curve measures the TPR (y-axis) versus the FPR (x-axis) at different threshold settings. The area under the ROC curve is denoted by AUC. The higher the value of AUC, the better the performance of the risk prediction model.

In order to verify the effectiveness and advantages of our proposed method, we compare our prediction model with the radiomics-features-based method [23] and CNN-based model mentioned in [17]. Our datasets do not include the records of clinical features as [17]. We only use the CTA image features from the CNN network for PPVO risk prediction. We use two independent datasets to evaluate the performance of these three different methods. The ROC curves of three different methods on  $Data_1$  and  $Data_2$  are shown in Fig. 11, respectively. In addition, Table III also shows the recall, accuracy and F1-score of the three different methods. Fig. 11 and Table III show that our proposed model have better performance than the other two methods with the AUC values 0.879 and 0.870 on two different

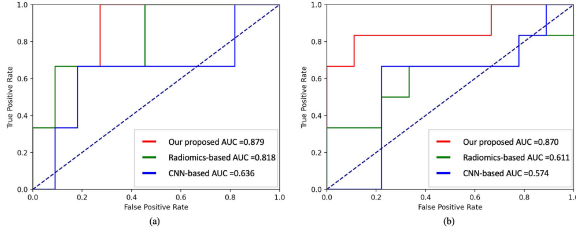


Fig. 11. The ROC curves of different prediction models on different datasets, (a):  $Data_1$ , (b):  $Data_2$ .

TABLE III  
PREDICTION PERFORMANCE OF DIFFERENT METHODS

		Radiomics-based [23]	CNN-based [17]	Our Proposed
AUC	$Data_1$	0.818	0.636	<b>0.879</b>
	$Data_2$	0.611	0.574	<b>0.870</b>
Recall	$Data_1$	0.667	0.667	<b>1.000</b>
	$Data_2$	0.500	0.500	<b>0.833</b>
Accuracy	$Data_1$	0.786	0.786	<b>0.786</b>
	$Data_2$	0.600	0.666	<b>0.733</b>
F1-score	$Data_1$	0.571	0.571	<b>0.667</b>
	$Data_2$	0.500	0.545	<b>0.714</b>

The bold entities mean the best results in comparison experiments.

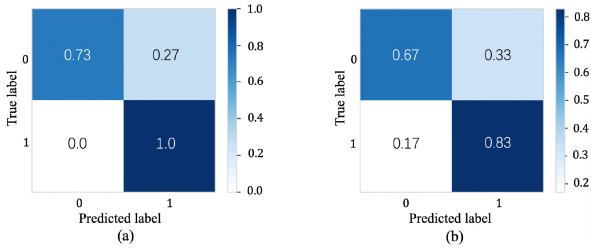


Fig. 12. The confusion matrix of the proposed prediction model on different dataset, (a)  $Data_1$ , (b)  $Data_2$ .

test datasets. It demonstrates the advantages of our prediction model.

The CNN is a black-box classifier, in which the features used for classification are not interpretable. The radiomics-features-based method constructs the prediction model through some complex radiomics features (such as texture features), but the texture features are usually not easy to understand. In addition, the proposed prediction model usually has stable performance on different CTA datasets, and is not affected by different CT scanning equipment and different scanning conditions. However, the performance of the other two PPVO classification methods in our experiments vary greatly.

These evaluation results indicate that the proposed risk prediction model can exhibit satisfactory performance in classifying patients on two independent datasets. In particular, the normalized confusion matrix shown in Fig. 12 shows that the prediction model can not only identify patients with PPVO with high precisions, but also recognize most of patients without PPVO.

An ablation study is experimented on  $Data_1$  to discuss the effect of the number of selected risk factors on classification performance of the prediction model. The results are shown in

TABLE IV  
ABLATION STUDY ABOUT THE EFFECT OF FEATURE NUMBER ON PREDICTION MODEL

Num	1	2	3	4	5	6
AUC	0.841	0.865	0.873	0.879	0.865	0.853
Num	7	8	9	10	11	12
AUC	0.881	0.861	0.813	0.786	0.786	0.762

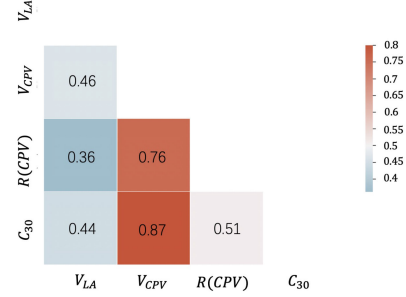


Fig. 13. The correlation between the selected risk factors.

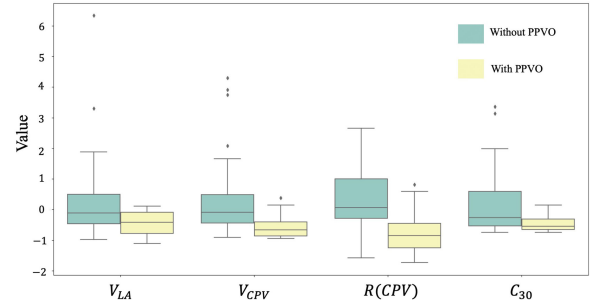


Fig. 14. Value distributions of four risk factors among patients without and with PPVO.

Table IV. Considering our small datasets, we choose four risk factors as the final risk factors to avoid over-fitting.

#### D. Properties of Risk Factors

Based on equation (11), if a patient has large CPV volume and LA volume and small DBLP, this patient has low risk of PPVO. The bigger the CPV average radius and CPV length are, the larger the CPV volume is. Fig. 13 shows the correlation between these four risk factors. While these risk factors have high correlations due to their definitions, they are actually complementary. For example, since the length of CPV is possibly short, it is not sufficient to correctly predict PPVO based only on the thickness of CPV ( $R(CPV)$ ). Additionally, even if the CPV is thicker and longer (i.e., with large volume  $V_{CPV}$ ), CPV is possibly far from LA. Thus, CPV volume  $V_{CPV}$  and  $C_{30}$  are useful complementary risk factors for  $R(CPV)$ . Here,  $V_{CPV}$  implicitly contains the information of CPV length. Based on  $Data_1$  and  $Data_2$ , the value distributions of each risk factor among patients without PPVO and with PPVO are shown in Fig. 14. It can be seen, while the four risk factors can be combined into the prediction model to distinguish between the

two classes, the average radius of CPV ( $R(CPV)$ ) itself can distinguish most PPVO patients.

#### IV. DISCUSSION

In this study, we propose a computational framework to explore high risk factors related to PPVO in TAPVC. Our main findings are as follows: 1) Four quantitative risk factors are discovered to be predictive of PPVO; 2) A risk prediction model is developed, being able to predict patients with high risk of PPVO; 3) A feasible computational framework is proposed to screen the risk factors for PPVO based on CTA images. More discussions are presented below.

##### A. On Clinical Importance

Based on the proposed risk prediction model, clinicians can recognize patients with high risk of PPVO. This helps clinicians in decision making and plan for follow-up procedures, such as carefully monitoring them after TAPVC repairing, and actively investigating their slightest suspicion of PPVO. In this way, clinicians can timely identify patients with PPVO symptoms and provide necessary treatments, such as the reoperation. Therefore, this risk prediction model is of great clinical significance in avoiding and reducing the death or sickness caused by PPVO.

##### B. On Risk Factors

In the past literatures, based on clinical experiences, clinicians have suggested some qualitative risk factors or observations [6], [8], [12], [14].

In this paper, four quantitative risk factors are discovered for PPVO. Compared with [12], we show that the volume of LA is an important risk factor. Younger ages generally correspond to smaller volumes of LA. Compared with the works [6], [8], [14] based on CPV only, we reveal that the average radius of CPV and CPV volume are important risk factors. The thicker the CPV, the smaller risk of PPVO. In [8] authors vaguely mentioned that anastomotic restriction is closely related to PPVO. Using the coupling feature  $C_{30}$ , we find it can quantify the extent of anastomosis. Thus, while we provide a quantitative calculation framework for clinical observations in literature, clinical observations as the evidence confirm our identified risk factors.

##### C. On Risk Prediction Model

Risk factors reported in [6], [8], [12], [14] may be related to PPVO classification. However, they are either qualitative and unclear to provide quantitative calculations, or they can only provide very few risk factors for PPVO predictions. Hence, a high-accuracy risk prediction model usually cannot be constructed based on the risk factors suggested in [6], [8], [12], [14]. Based on the four risk factors discovered in this paper, a risk prediction model is constructed, which can provide a quantitative and high-accuracy risk assessment of PPVO. The prediction model shows how the risk prediction is impacted by the four risk factors. The four risk factors have different contributions to the prediction model as shown in equation (11) and Fig. 15. The larger value of each risk factor, the lower the risk probability is.

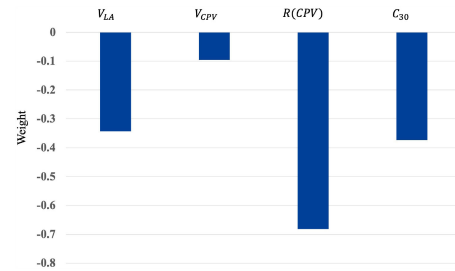


Fig. 15. The contributions of four different risk factors in prediction model.

TABLE V  
SEGMENTATION PERFORMANCE OF DIFFERENT METHODS

		DSC	ASD (mm)	HD (mm)
Our model (SCAB-VNet)	PV	<b>0.772±0.136</b>	<b>0.926 ±0.973</b>	<b>13.398±7.565</b>
	LA	<b>0.814±0.138</b>	<b>0.942±1.860</b>	<b>8.448±8.237</b>
V-Net [30]	PV	0.727±0.175	1.605±2.388	13.542±7.004
	LA	0.764±0.143	1.366±2.278	9.821±7.491
3D-UNet [43]	PV	0.700±0.166	1.846±5.160	14.213±7.982
	LA	0.738±0.148	1.456±2.169	9.624±6.675

The bold entities mean the best results in comparison experiments.

The proposed prediction model provides the probability of risk in developing PPVO. The sensitivity of the model depends on the setting of a low or high probability threshold. Setting to low threshold has pros and cons. On one hand, a lower threshold can increase sensitivity (lower specificity) and trigger more clinical evaluations or surveillance for patients at risk, thereby leading to timely re-intervention and reducing PPVO-related mortality. On the other hand, for patients without PPVO, this can cause extra costs in unnecessary workups attributed to rigorous assessments. Additionally, the misdiagnosis in some instances can potentially cause some anxiety for patients' families in the short term but that is much less severe than misdiagnosis which results in death. Nevertheless, the risk of misdiagnosis can be mitigated because the diagnosis of PPVO can be based on a comprehensive evaluation of CT, echocardiography, and clinical manifestations rather than on imaging criteria alone. In the future, we will further improve the accuracy of risk prediction to reduce misdiagnosis by integrating with other clinical data.

##### D. On the Computational Framework

It is important to segment LA and PV from CTA images with high accuracy and efficiency [42]. We use dice similarity coefficient (DSC), average surface distance (ASD), and Hausdorff distance (HD) to evaluate the SCAB-VNet. We evaluate its performance through 5-fold cross-validation on  $Data_1$  and compare it with the V-Net [30] and 3D-UNet [43], which are commonly used in segmentation tasks. According to the result shown in Table V, SCAB-VNet has better performance than the V-Net and 3D-UNet. It has higher DSC values and lower ASD and HD values than V-Net and 3D-UNet, with an average DSC of 0.772 (PV) and 0.814 (LA). This means that SCAB-VNet has better segmentation results in terms of both regions and boundaries. SCAB-VNet takes about 400 milliseconds to generate segmentation results for LA and PV from a 3D CTA image. Nevertheless, SCAB-VNet usually only provides some

TABLE VI

CLASSIFICATION PERFORMANCE OF DIFFERENT PREDICTION MODELS WITH CLINICAL FACTORS

		11 Clinical features	15 Hybrid features	8 Hybrid features	Our proposed
AUC	<i>Data</i> <sub>1</sub>	0.848	0.621	0.848	<b>0.879</b>
	<i>Data</i> <sub>2</sub>	0.500	0.769	0.759	<b>0.870</b>

The bold entities mean the best results in comparison experiments.

rough segmentation results. Therefore, clinicians need to further manually correct such vague segmentation errors in different slices based on their experiences. This usually requires an average of 20 minutes per each CTA data. This is more efficient than a complete manual delineation that takes more than 100 minutes. Therefore, considering both the accuracy and time, the hybrid segmentation strategy in this paper is an effective and time-saving method.

The risk factors described by clinicians and discussed in literature are qualitative, which may lead to ambiguity in application and practice. In this paper, we design quantitative ways to compute them, leading to a feature pool shown in Section II-B. In addition, novel features such as the histogram-based DBLP and coupling features are incorporated. Based on such quantitative features, we can extract quantitative risk factors with machine learning methods and build the risk prediction model for accurate diagnosis.

### E. On Interpretability and Repeatability

In tumor study, the radiomics features [23] selected from CTA images are usually complex texture features, which are not easy to understand. Texture features describe image details, but image details are easily affected by different CT scanning equipment and different scanning conditions. Therefore, the performance of the prediction model based on radiomics features vary greatly in our experiment. However, in our method, the selected morphological features do not change in different CTA datasets, which makes our prediction model have a stable performance in different CTA datasets. The morphological-features-like risk factors and their risk prediction model can be easy to understand and have good interpretability and reproducibility.

### F. On the Clinical Features

11 clinical features, including sex, weight, height, age, preoperative SPO<sub>2</sub>, delayed closure, hospital stay, cardiopulmonary bypass time (CPB), temperature during cardiopulmonary bypass, ICU stay, preoperative PVO, are also considered. Among them, four clinical features, such as weight, hospital stay, CPB and sex, were applied in [17]. Similar to our proposed model, three PPVO prediction models can also be constructed respectively by 11 clinical features, 15 hybrid features (11 clinical features and the four selected risk factors), and 8 hybrid features (four clinical features used in [17] and the four selected risk factors). The AUC of these prediction models in *Data*<sub>1</sub> and *Data*<sub>2</sub> are shown in Table VI. Compared with these three models, our

proposed model has better performance. In the future, we will collect more subjects to discuss the impact of clinical factors.

## V. CONCLUSION

In this paper we propose a computational framework to measure quantitative risk factors from CTA images and use them to build a risk prediction model for postoperative PVO in TAPVC patients. Qualitative risk descriptions in the literature can now be quantified in a rigorous way. Based on the extracted features, the prediction model can assess the risk of postoperative PVO with high accuracy. The approach in this work has great clinical impact by avoiding or reducing the death rate caused by postoperative PVO. In the future, we will collect more multi-center data to further validate the effectiveness of our model and advance the clinical application of our model in TAPVC patients.

## REFERENCES

- [1] J. R. Herlong, J. J. Jagers, and R. M. Ungerleider, "Congenital heart surgery nomenclature and database project: Pulmonary venous anomalies," *Ann. Thoracic Surg.*, vol. 69, no. 3, pp. 56–69, 2000.
- [2] "Facts about total anomalous pulmonary venous return or TAPVR," *Centers Dis. Control Prevention*, Nov. 17, 2020. [Online]. Available: <https://www.cdc.gov/ncbddd/heartdefects/tapvr.html>
- [3] J. T. Burroughs and J. E. Edwards, "Total anomalous pulmonary venous connection," *Amer. Heart J.*, vol. 59, no. 6, pp. 913–931, 1960.
- [4] B. Yanagawa *et al.*, "Primary sutureless repair for 'simple' total anomalous pulmonary venous connection: Midterm results in a single institution," *J. Thoracic Cardiovasc. Surg.*, vol. 141, no. 6, pp. 1346–1354, 2011.
- [5] J. D. S. Louis *et al.*, "Repair of 'simple' total anomalous pulmonary venous connection: A review from the pediatric cardiac care consortium," *Ann. Thoracic Surg.*, vol. 94, no. 1, pp. 133–138, 2012.
- [6] K. Bando *et al.*, "Surgical management of total anomalous pulmonary venous connection. Thirty-year trends," *Circulation*, vol. 94, no. 9 Suppl, pp. II12–6, 1996.
- [7] R. K. Lamb, S. A. Qureshi, J. L. Wilkinson, R. Arnold, D. I. Hamilton, and C. R. West, "Total anomalous pulmonary venous drainage: Seventeen-year surgical experience," *J. Thoracic Cardiovasc. Surg.*, vol. 96, no. 3, pp. 368–375, 1988.
- [8] G. Shi *et al.*, "Total anomalous pulmonary venous connection: The current management strategies in a pediatric cohort of 768 patients," *Circulation*, vol. 135, no. 1, pp. 48–58, 2017.
- [9] F. Lacour-Gayet, "Surgery for pulmonary venous obstruction after repair of total anomalous pulmonary venous return," in *Seminars in Thoracic and Cardiovascular Surgery: Pediatric Cardiac Surgery Annual*, vol. 9, no. 1. Amsterdam, The Netherlands: Elsevier, 2006, pp. 45–50.
- [10] N. Yoshimura *et al.*, "Current topics in surgery for isolated total anomalous pulmonary venous connection," *Surg. Today*, vol. 44, no. 12, pp. 2221–2226, 2014.
- [11] A. N. Seale *et al.*, "Total anomalous pulmonary venous connection: Morphology and outcome from an international population-based study," *Circulation*, vol. 122, no. 25, pp. 2718–2726, 2010.
- [12] T. Karamlou *et al.*, "Clinical perspective," *Circulation*, vol. 115, no. 12, pp. 1591–1598, 2007.
- [13] C. L. H. Friesen *et al.*, "Total anomalous pulmonary venous connection: An analysis of current management strategies in a single institution," *Ann. Thoracic Surg.*, vol. 79, no. 2, pp. 596–606, 2005.
- [14] K. J. Jenkins, P. Sanders, E. J. Orav, E. A. Coleman, J. E. Mayer, and S. D. Colan, "Individual pulmonary vein size and survival in infants with totally anomalous pulmonary venous connection," *J. Amer. College Cardiol.*, vol. 22, no. 1, pp. 201–206, 1993.
- [15] R. C. Deo, "Machine learning in medicine," *Circulation*, vol. 132, no. 20, pp. 1920–1930, 2015.
- [16] X. Hu *et al.*, "Joint clinical data and CT image based prognosis: A case study on postoperative pulmonary venous obstruction prediction," in *Proc. Int. Workshop PRedictive Intell., MEDicine*, Springer, 2020, pp. 58–67.
- [17] Z. Yao *et al.*, "A machine learning-based pulmonary venous obstruction prediction model using clinical data and CT image," *Int. J. Comput. Assist. Radiol. Surg.*, vol. 16, no. 4, pp. 609–617, 2021.

- [18] S. C. Siu *et al.*, "Prospective multicenter study of pregnancy outcomes in women with heart disease," *Circulation*, vol. 104, no. 5, pp. 515–521, 2001.
- [19] S. B. Puchner *et al.*, "High-risk plaque detected on coronary ct angiography predicts acute coronary syndromes independent of significant stenosis in acute chest pain: Results from the Romicat-II trial," *J. Amer. College Cardiol.*, vol. 64, no. 7, pp. 684–692, 2014.
- [20] M. Károlyi *et al.*, "Quantitative CT assessment identifies more heart transplanted patients with progressive coronary wall thickening than standard clinical read," *J. Cardiovasc. Computed Tomogr.*, vol. 13, no. 2, pp. 128–133, 2019.
- [21] J. Wu *et al.*, "Ascending aortic length and risk of aortic adverse events," *J. Amer. College Cardiol.*, vol. 74, 2019, Art. no. 1883.
- [22] P. Lambin *et al.*, "Radiomics: Extracting more information from medical images using advanced feature analysis," *Eur. J. Cancer*, vol. 48, no. 4, pp. 441–446, 2012.
- [23] H. J. Aerts *et al.*, "Decoding tumour phenotype by noninvasive imaging using a quantitative radiomics approach," *Nature Commun.*, vol. 5, no. 1, pp. 1–9, 2014.
- [24] Y.-Q. Huang *et al.*, "Development and validation of a radiomics nomogram for preoperative prediction of lymph node metastasis in colorectal cancer," *J. Clin. Oncol.*, vol. 34, no. 18, pp. 2157–2164, 2016.
- [25] I. Cetin *et al.*, "A radiomics approach to computer-aided diagnosis with cardiac cine-mri," in *Proc. Int. Workshop Stat. Atlases Comput. Models Heart*. Springer, 2017, pp. 82–90.
- [26] M. Kolossváry, M. Kellermayer, B. Merkely, and P. Maurovich-Horvat, "Cardiac computed tomography radiomics," *J. Thoracic Imag.*, vol. 33, no. 1, pp. 26–34, 2018.
- [27] M. Kolossváry and P. Maurovich-Horvat, "Cardiac CT Radiomics," in *CT of the Heart*. Berlin, Germany: Springer, 2019, pp. 715–724.
- [28] E. K. Oikonomou *et al.*, "A novel machine learning-derived radiotranscriptomic signature of perivascular fat improves cardiac risk prediction using coronary CT angiography," *Eur. Heart J.*, vol. 40, no. 43, pp. 3529–3543, 2019.
- [29] R. J. Gillies, P. E. Kinahan, and H. Hricak, "Radiomics: Images are more than pictures, they are data," *Radiol.*, vol. 278, no. 2, pp. 563–577, 2016.
- [30] F. Milletari, N. Navab, and S.-A. Ahmadi, "V-Net: Fully convolutional neural networks for volumetric medical image segmentation," in *Proc. IEEE 4th Int. Conf. 3D Vis.*, 2016, pp. 565–571.
- [31] J. Li, H. Chen, F. Zhu, C. Wen, H. Chen, and L. Wang, "Automatic pulmonary vein and left atrium segmentation for TAPVC preoperative evaluation using V-net with grouped attention," in *Proc. 42nd Annu. Int. Conf. IEEE Eng. Med. Biol. Soc.*, 2020, pp. 1207–1210.
- [32] L. Itti, C. Koch, and E. Niebur, "A model of saliency-based visual attention for rapid scene analysis," *IEEE Trans. Pattern Anal. Mach. Intell.*, vol. 20, no. 11, pp. 1254–1259, Nov. 1998.
- [33] N. Otsu, "A threshold selection method from gray-level histograms," *IEEE Trans. Syst., Man, Cybernet.*, vol. 9, no. 1, pp. 62–66, Jan. 1979.
- [34] V. Caselles, R. Kimmel, and G. Sapiro, "Geodesic active contours," *Int. J. Comput. Vis.*, vol. 22, no. 1, pp. 61–79, 1997.
- [35] W. E. Lorensen and H. E. Cline, "Marching cubes: A high resolution 3D surface construction algorithm," *ACM Siggraph Comput. Graph.*, vol. 21, no. 4, pp. 163–169, 1987.
- [36] S. Bouix, K. Siddiqi, and A. Tannenbaum, "Flux driven automatic centerline extraction," *Med. Image Anal.*, vol. 9, no. 3, pp. 209–221, 2005.
- [37] B. H. Menze *et al.*, "A comparison of random forest and its gini importance with standard chemometric methods for the feature selection and classification of spectral data," *BMC Bioinf.*, vol. 10, no. 1, pp. 1–16, 2009.
- [38] M. Kuhn and K. Johnson, "An introduction to feature selection" in *Applied Predictive Modeling*. Springer, 2013, pp. 487–519.
- [39] S. Wu *et al.*, "A radiomics nomogram for the preoperative prediction of lymph node metastasis in bladder cancer," *Clin. Cancer Res.*, vol. 23, no. 22, pp. 6904–6911, 2017.
- [40] W. Sauerbrei, P. Royston, and H. Binder, "Selection of important variables and determination of functional form for continuous predictors in multivariable model building," *Statist. Med.*, vol. 26, no. 30, pp. 5512–5528, 2007.
- [41] D. W. Hosmer and S. Lemeshow, "Goodness of fit tests for the multiple logistic regression model," *Commun. Statist.-Theory Methods*, vol. 9, no. 10, pp. 1043–1069, 1980.
- [42] X. Zhuang *et al.*, "Evaluation of algorithms for multi-modality whole heart segmentation: An open-access grand challenge," *Med. Image Anal.*, vol. 58, 2019, Art. no. 101537.
- [43] Ö. Çiçek, A. Abdulkadir, S. S. Lienkamp, T. Brox, and O. Ronneberger, "3D U-Net: Learning dense volumetric segmentation from sparse annotation," in *Proc. Int. Conf. Med. Image Comput. Comput.- Assist. Interv.*, Springer, 2016, pp. 424–432.